Design and Nonlinear Servo Control of MEMS Mirrors and Their Performance in a Large Port-count Optical Switch

P. B. Chu, I. Brener, C. Pu, S-S. Lee, J.I. Dadap, S. Park, K. Bergman, N. Bonadeo, T. Chau, M. Chou, R. Doran, R. Gibson, R. Harel, J. J. Johnson, C. D. Lee, D. R. Peale, B. Tang, D. Tong, M. Tsai, Q. Wu, W. Zhong, E. L. Goldstein, L. Y. Lin, and J. A. Walker

Tellium Inc., 2 Crescent Place, Oceanport, New Jersey 07757

***Abstract*—We demonstrate full closed-loop control of electrostatically actuated double-gimbaled MEMS mirrors and use them in an optical cross-connect. We show switching times of less than 10 ms and optical power stability of better than 0.2 dB. The mirrors, made from 10 μm thick single-crystal silicon and with a radius of 400-450 μm, are able to tilt to 8° corresponding to 80% of touchdown angle. This is achieved using a nonlinear closed-loop control algorithm, which also results in a maximum actuation voltage of 85 V, and a pointing accuracy of less than 150 μrad. This paper will describe the MEMS mirror and actuator design, modeling, servo design, and measurement results.**

***Index Terms*—MEMS, electrostatic actuator, nonlinear closed-loop control, snap-down, torsional spring, optical cross-connects.**

I. INTRODUCTION

In high port-count 3D-MEMS optical crossconnects (OXC) [1], one is typically faced with the challenge of achieving as large a mirror angular swing as possible with a minimum separation between the ports to achieve high port-count and low optical loss. Most MEMS-based OXCs demonstrated to date use an open-loop architecture in mirror position control [2], [3], [4], [5]. Optical power monitoring through each connection can provide certain feedback for mirror reference positions, but this is a slow process and does not provide direct mirror position control.

The physics of an electro-statically actuated MEMS gimbal mirror dictates that the tilting mirror becomes unstable at a certain angle commonly referred to as the “snap-down” angle [6], [7], which lies between 1/3 and 1/2 of the mirror "touchdown” angle (i.e., when the mirror plate physically contacts the underlying electrodes). This instability phenomenon is similar to non-tilting electrostatic actuators used in MEMS sensors and micro-robotics [8], [9]. Under open-loop control, the mirror tilt angle is usually limited to less than a third of the touchdown angle. Due to this unstable behavior of electrostatic actuators, the physical air gap employed may need to be more than three times larger than the minimum gap needed to achieve the desired physical swing angle, thus resulting in unnecessarily high drive voltages.

One method used to extend the stable operating range is to reduce the electrode radius toward the axis of rotation [10], but this method inevitably leads to lower torque (and a higher drive voltage). Using vertical electrodes working in conjunction with traditional electrodes is an effective way to increase snap-down angle [11], [12]. Depending on the implementation, this approach may require complex fabrication process, asymmetric devices [11], and potentially higher device cost.

Additional complexity in OXC systems arises from the extremely high pointing accuracy required, regardless of the technology used. Typically, an angular misalignment of the order of 100 μrad is enough to increase the optical loss by a fraction of a dB. Maintaining such a pointing accuracy of MEMS mirrors over long periods of time is a big challenge. Also, stochastic perturbations such as shock and vibration can introduce mechanical misalignment into the mirror position leading to severe penalties in optical performance.

All of these issues can be eliminated through the use of active position control of the MEMS mirrors. Servo controlled mirrors can be actuated far beyond the snap-down angle [13], [14], [15], thereby reducing the required air gap and thus drive voltage. By employing the MEMS mirror design and servo controller described in this paper, we are able to extend the operation range of the mirror from a snap down tilt angle of <4° to a little over 8°, which is ~80% of the mirror “touchdown” angle (of 10.3°), with less than 100 V. Servo control also provides corrective action needed to eliminate position drifts that arise from either internal mechanisms, such as charge build-up, or external perturbations, such as vibration or shock.

In addition to the servo considerations mentioned above, an ideal MEMS mirror for optical switching applications would have the following merits: *light and rigid*—for vibration and shock immunity; *flat, large and high-reflective surface*—for low optical loss; *simple and repeatable motion*—for high manufacturing yield and long-term stability; and *linear and* *uncoupled motion*—for simple control. These criteria govern the design parameters for our MEMS mirrors needed to achieve high performance MEMS-based OXCs.

The next section describes the fabrication and design of the MEMS mirrors used in this work. Details of the different components of the mirror (mirror structure, actuator, and springs) will be given. In the subsequent sections, we describe the nonlinear electromechanical modeling of the mirror, followed by the nonlinear controller algorithm and the performance of a single MEMS mirror under servo control. Finally the switching and operation performance of servo-controlled MEMS mirrors inside an OXC will be presented.

II. MEMS MIRROR DESIGN AND SIMULATION

A. *Mirror Fabrication and Design*

The MEMS mirrors used in this work are fabricated using Analog Devices' proprietary optical iMEMS process [16], [17]. Optical iMEMS is an SOI (Silicon-on-insulator) based three-layer process with the sandwiched silicon spacer as the sacrificial layer. This process provides the advantages of both bulk and surface silicon micromachining technologies. An illustration of the cross-section of a MEMS mirror designed for this process is shown in Figure 1.

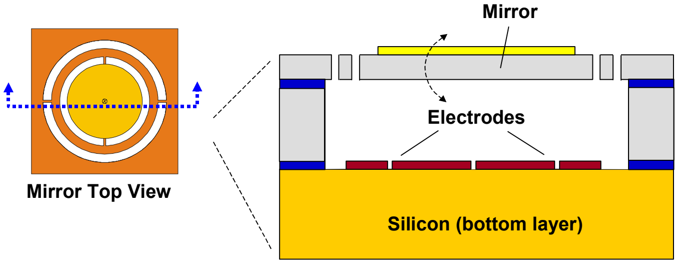

Figure 1: Schematic cross-section of an electrostatic micro-mirror

Single crystal silicon (SCS) is the material of choice to achieve mechanically robust springs in order to meet rigorous reliability requirements [18]. SCS also yields a thin but nearly stress-free and sufficiently rigid bulk substrate for the mirror. Typical mirrors used in this work have a thickness of 10µm, with radius from 400 to 450µm. This same SCS layer can be used to fabricate precision high- and low-voltage BiCMOS circuitry [17].

A scanning electron microscopy (SEM) micrograph of a fabricated MEMS mirror is shown in Figure 2. One pair of springs (gimbal axis) connects the gimbal ring to the fixed surrounding structure and the other pair (mirror axis) connects the mirror plate to the gimbal ring. The mirror axis springs penetrate into the mirror structure in order to yield a gimbal with a simple circular shape and to reduce the overall mirror weight. The additional optical loss due to the penetrating mirror axis springs is only 0.3 dB by optical beam propagation analysis.

Surrounding the mirror is a trench realized with the same conductive polysilicon as the vias connecting the top circuitry to the bottom electrodes. The trench, which is initially covered with oxide, forms a critical chemical barrier for the bulk silicon substrate during the XeF_2 [19] sacrificial etch of the material underneath the MEMS mirror. The trench also serves several other purposes during operation: i) It is used to isolate individual mirrors from each other when an array is fabricated; and ii) it is also used to define the boundary of the volume of the air pocket underneath the mirror, thus controlling the mirror quality factor, Q [20].

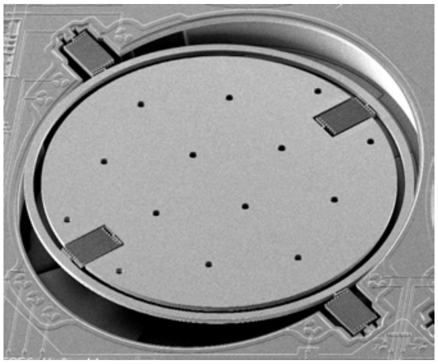

Figure 2: SEM micrograph of a fabricated MEMS mirror

In order to achieve the desired optical reflectivity, a thin 700-Angstrom-thick layer of gold is evaporated on the top surface of the mirrors. When coated with gold on one side, these mirrors were found to have a typical radius of curvature greater than 30 cm under normal operating conditions, and with a typical reflectivity of 97% for wavelengths of interest (λ = 980nm, 1310nm, and 1550nm). The torsional mirrors show typical resonant frequencies at 0° deflection angle between 300 and 400 Hz (both axes), and a quality factor (Q) of 3 ~ 5 in air. The low Q value of the mirror is realized primarily by the damping force of the air under the mirror. This low Q value improves the mirror dynamics significantly, as will be discussed later.

B. *Actuator Design*

In theory, three electrodes are adequate for controlling a two-axis gimbaled mirror. However, the symmetry of a four-electrode design helps to decouple the motion of the two axes and thus simplifies the control algorithm. Therefore, the MEMS mirror presented here is actuated through the application of voltages to four electrodes located 80µm underneath the mirror with an illustrative geometry shown in Figure 3. Every quadrant electrode can be further divided in an optimal fashion between driving and sensing electrode if capacitive sensing is required. The sensing portion may be used for angular sensing through differential-capacitance measurements using on-chip circuitry [21].

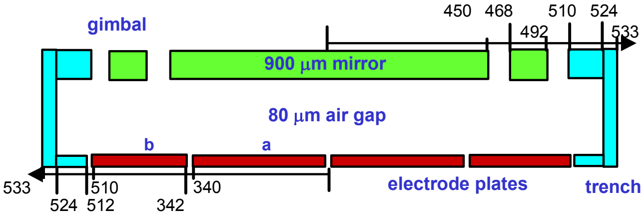

Figure 3: Schematic diagram of a MEMS mirror with design dimensions

The optimization of the electrode design is based on tradeoffs between several primary considerations, including linearity and resolution for drive torque and sense capacitance as functions of voltages and tilt angles, and maximum drive voltage needed to move the mirror between any two arbitrary angles. Other considerations include switching time (governed by magnitude of electrostatic torques and mechanical properties like spring constant and Q), position resolution and stability (dependent on actuator linearity, torque and capacitance look-up table implementation, A/D and D/A resolution, and so forth), and electronics reliability (maximum drive voltage).

The desired maximum actuation voltage for our mirror designs is 85V. This voltage value is selected for electronics circuitry reliability, MEMS device reliability, electronics drift, and noise considerations. Depending on the specific mirror design, this maximum voltage takes into account an additional 10% to 25% margin for servo performance optimization in addition to the maximum open-loop snap-down voltage.

In the segmented electrode design shown in figure 3, both inner and outer electrodes can serve for either driving the mirror or sensing the mirror angle. Inner electrodes typically offer better linearity in terms of capacitance and rate of change in capacitance as a function of tilt angle compared to outer electrodes. One of the main reasons for this effect is a slower change of the average gap between the mirror and the electrodes as a function of tilt angle for inner electrodes.

Linearity in the capacitance is desirable for capacitive sensing so that the tilt angle can be readily estimated from the measured capacitance without complex look-up tables or conversion functions, which may introduce error in the angle estimate for feedback. On the other hand, linearity in the rate of change in capacitance is desirable for actuation because electrostatic torque is a function of the derivative of the capacitance with respect to the MEMS angle instead of the capacitance. For this reason, the inner electrodes seem suitable for both actuation and sensing.

For actuation, however, additional considerations are required. The distance R from the center creates a level arm effect: larger R could lead to larger torque for the same area of electrode. For this reason, the outside electrodes are particularly suitable for actuation, especially if drive voltage is to be minimized. The tradeoff for large torque is a less optimized linearity in terms of torque as a function of tilt angle and reduced open-loop stability. “Outside-drive” tends to yield smaller snap-down angles. In fact, it is possible to design an “inside-drive” configuration with no snap-down angle (i.e., the mirror touches down before it can snap down). In this case, several hundred volts may be needed to tilt the mirror to a large angle.

In our design, we make use of “outside-drive” to ensure the maximum voltage requirement of less than 85V. Simulations, employing finite element analysis (FEA), of the relation between the applied voltage and tilt angle for mirror and gimbal axes are shown in Figure 4 for one of our mirror designs. This particular mirror design has a 900-μm-diameter mirror with 24-μm-wide gimbal ring. It has an axial spring constant of 3.314x 10^{-9} N/m for both mirror and gimbal axes.

The simulations show that the angles as functions of the applied voltages are highly non-linear. For each axis, the required voltage is monotonically increasing for angles smaller than the pull-in angle (about 4°). For larger angles, monotonically decreasing amplitudes of voltages are needed.

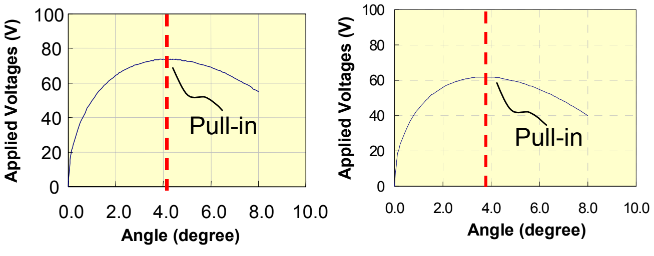

(a) (b)

Figure 4: FEA simulation of open-loop actuation voltage versus tilt angle for a 900μm diameter MEMS mirror about the mirror (a) and gimbal (b) axes. Note that less voltage is required for the gimbal axis.

C. *Spring Design*

As described earlier, there are two pairs of springs for each MEMS mirror, the mirror and the gimbal axes. Spring design impacts all aspects of mirror performance. Both stiffness and mode frequencies of a spring are important design factors in addition to physical form factor. Precision engineering of spring stiffness improves mirror controllability. Spring size may also affect optical reflectivity.

All the mirror structures are fabricated on the top 10-μm-thick SCS layer. Therefore, the springs must have the same thickness of 10 μm. Restriction in this one geometric dimension imposes a great challenge to design a soft torsional spring. For example, a straight tether spring would be several millimeters long in order to maintain the maximum operating voltage under 85V. Such a design is impractical since the springs would be longer than the diameter of mirror itself. The only way to overcome this limitation is to *fold* the long straight spring into a serpentine shape.

1) *Two Configurations of Serpentine Springs*

There are two possible ways to fold a string spring into a serpentine shape: long elements can be either aligned to or perpendicular to the axis of rotation. A spring with the long elements normal to the axis of rotation is called *orthogonal serpentine torsional spring* (OSTS), and a spring with its long elements arranged parallel to the axis of rotation is called *parallel serpentine torsional spring* (PSTS). Figure 5 shows serpentine springs with two different configurations.

The two spring configurations offer distinct mirror performance. The OSTS and PSTS in the figure may be designed to obtain the same torsional mode frequency; however there would be a large difference in their sizes. In fact, the size of an OSTS is twice as large as a PSTS with the same fundamental mode frequency. In addition to the size advantage, the fundamental mode of a PSTS is always the torsional mode, while this is not the case for an OSTS. This is due to the difference in their fundamental working principle. In the OSTS case, the bending mode of long spring elements contributes to the majority of its torsional mode and the bending stiffness is proportional to the cubic power of its thickness (stiffness $\equiv k_{OSTS} \propto w \cdot t^3$, where t is the beam thickness and w is the beam width). In the PSTS case, the torsional mode of individual long spring elements contributes to the torsional mode and torsional stiffness is directly proportional to its thickness ($k_{PSTS} \propto w^3 t$). In our design, $w = 2$ µm and $t = 10$ µm.

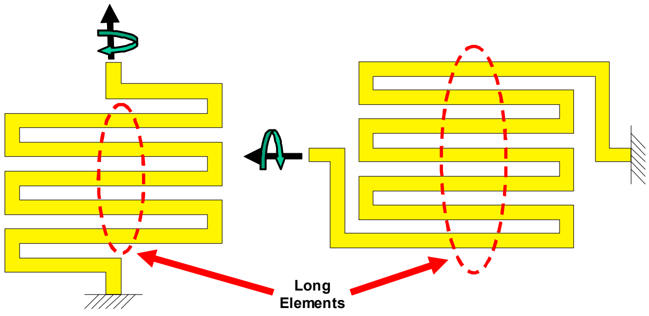

(a) (b)

Figure 5: Two configurations of serpentine springs with long spring members (a) orthogonal, and (b) parallel to axis of rotation.

Typical mode frequencies (ANSYS simulation results) of OSTS and PSTS designs are tabulated in Table 1. In both cases, an 800-µm-diameter, 10-µm-thick mirror structure is used in the simulation. Even though both designs have the same fundamental mode, unlike the OSTS design, the fundamental mode of the PSTS design is indeed the torsional mode as desired.

Mode /Type	Funda-mental (Hz)	1st Higher (Hz)	2nd Higher (Hz)	3rd Higher (Hz)
OSTS	393 (y-disp.)	471 (z-disp.)	522 (x-disp.)	579 (torsional)
PSTS	394 (torsional)	2239 (y-disp.)	3561 (z-disp.)	3614 (x-disp.)

Table 1: Mode frequency simulation results of OSTS and PSTS configurations having the same fundamental frequency. The x and y axes are in the plane of the mirror and z is the out-of-plane axis, orthogonal to the mirror plane.

2) *Enhanced PSTS*

A typical PSTS is found to have a relatively high mode frequency ratio. The mode frequency ratio is defined as the ratio of the first higher mode frequency to the fundamental mode frequency. Since only the torsional modes of the MEMS mirrors are useful in optical beam steering, it is undesirable to have torsional motions exciting the higher modes. Therefore, the mode frequency ratio ideally should be as high as possible.

ANSYS modeling shows that in the PSTS design these short spring elements have insignificant contribution to the torsional resonant frequency but have more effect on the higher modes. By stiffening the short spring elements, the torsional mode frequency is unchanged, while the other mode frequencies are increased. Therefore, the mode frequency ratio is further improved. When widening the short spring elements from 2 µm to 4 µm, the mode frequency ratio increased by 8% without any other penalty. However, no additional benefit is found for widths beyond 4 µm.

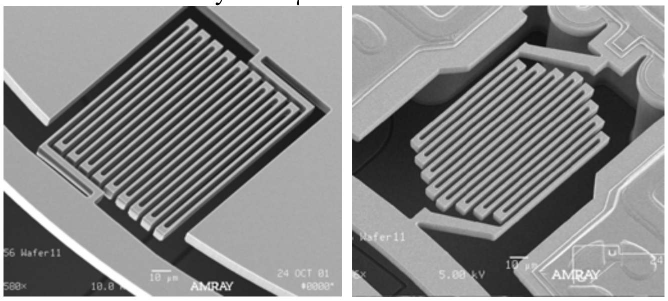

(a) (b)

Figure 6: SEM micrographs of enhanced (a) rectangular PSTS and (b) diamond PSTS

To further improve the mode frequency ratio, one can enhance the PSTS design by stiffening the short spring elements as shown in Figure 6 (a). As in the case of PSTS design, spring elements perpendicular to the axis of rotation have very small contribution to the fundamental mode (torsional mode).

3) *Enhanced Diamond-shaped PSTS*

The spring designs described so far have long elements with equal length, yielding an overall *rectangular* shape (RPSTS). The enhanced *diamond-shaped parallel serpentine torsional spring* (DPSTS) (Figure 6 (b)), which has an outline of a diamond shape, provides the best mechanical performance. Extensive ANSYS simulations show that the outer elements of a PSTS contribute more to higher mode frequencies and have less effect on the fundamental frequency. Therefore, tapering (gradually shortening) the lengths of the outer elements of the spring yields a higher mode frequency ratio while maintaining a similar value of the fundamental mode. Typical improvement in mode frequency ratio is 5~10%.

This improvement, however, comes with a penalty. Since the outer spring elements have non-zero contribution to the resonant frequency, the center spring element has to be lengthened in order to compensate the tapering of the outer spring elements. Therefore, a DPSTS is longer than an RPSTS design even though they have comparable overall area. This could cause an additional 0.2 dB optical loss. To minimize optical loss we chose an enhanced RPSTS as the preferred springs for our final mirror design.

III. ELECTROMECHANICAL MODELING

As already mentioned, the electrostatically actuated gimbaled mirror is inherently nonlinear in its actuation. Moreover, the angular sensing scheme can also have a nonlinear response, especially when differential capacitance is used for measuring angles. In order to make the control problem manageable, a number of simplifying assumptions are made regarding the plant to be controlled.

The assumptions are the following: i) Only torsional motions are significant; all other motions from higher-order modes are neglected; (ii) the torsional springs have a linear angle and torque relationship; iii) all inter-axis mechanical coupling are negligible (but not the coupling in the electrostatic torque); iv) all electrostatic action on the mirror springs is small; v) the mirror damping is independent of angle; and vi) the moments of inertia of the mirror are independent of angles. We expect that the deviations from the ideal cases above, i.e., higher-order effects and nonlinearities, are minimal such that they can be bundled as phase margin that a good closed-loop servo design can account for.

We now consider the electro-mechanics of our system. Let X and Y denote the mirror and gimbal axes, respectively; while α and β denote the angles around the gimbal (Y) and mirror (X) axes respectively. The equations of motion can then be expressed as

$$J_Y \ddot{\alpha} + \gamma_Y \dot{\alpha} + K_Y \alpha = T_Y(\alpha,\beta,V_1,V_2,V_3,V_4)$$

$$J_X \ddot{\beta} + \gamma_X \dot{\beta} + K_X \beta = T_X(\alpha,\beta,V_1,V_2,V_3,V_4) \quad (1)$$

Here, $T_{X,Y}(\alpha,\beta,V_1,V_2,V_3,V_4)$ are the electrostatic torques, $\gamma_{X(Y)}$ the damping parameters, $J_{X(Y)}$ the moments of inertia, and $K_{X(Y)}$ the torsional spring stiffness. We calculate $J_{X(Y)}$ purely from geometrical factors and also by modeling software. We extract $K_{X(Y)}$ and $\gamma_{X(Y)}$ from experimental measurements, by driving each axis with a low-amplitude, chirped, sinusoidal voltage around $\alpha = \beta = 0°$, and by subsequently fitting these two parameters.

Equations (1) describe a classical two-dimensional, second-order linear system, for which well-known linear control techniques can be used to design a controller using torque as the control variable [22]. The torques $T_{X,Y}(\alpha,\beta,V_1,V_2,V_3,V_4)$ depend in a nonlinear fashion on the two angles and four electrode voltages, which are the actual control inputs to the electrostatic system. If one can establish a good knowledge of this nonlinearity, then the necessary applied voltages can then be determined using an inverse torque function.

From symmetry considerations, we can approximate the electrostatic torques with the following formulas:

$$\begin{aligned} &T_X(\alpha,\beta,V_1,V_2,V_3,V_4) \\ &= f(\alpha,\beta)V_4^2 + f(-\alpha,\beta)V_3^2 - f(-\alpha,-\beta)V_2^2 - f(\alpha,-\beta)V_1^2 \\ &T_Y(\alpha,\beta,V_1,V_2,V_3,V_4) \\ &= g(\alpha,\beta)V_4^2 - g(-\alpha,\beta)V_3^2 - g(-\alpha,-\beta)V_2^2 + g(\alpha,-\beta)V_1^2 \end{aligned} \quad (2)$$

where $f(\alpha,\beta) = (1/2)\partial C/\partial\beta$ and $g(\alpha,\beta) = (1/2)\partial C/\partial\alpha$, and $C = C(\alpha,\beta)$ is the driving electrode capacitance with respect to the mirror node (it is assumed to be the same for all quadrants).

Under servo operation, the torques $T_{X,Y}(\alpha,\beta,V_1,V_2,V_3,V_4)$ are calculated by the controller. Then one needs to find a combination of voltages that will provide these torques. Eqs. (2) represents two equations with four variables to solve ($V_{1\ldots4}$), and thus the system is under-determined. A possible solution to Eq. (2) is to require that at any given time, at most two voltages are non-zero. This solution reduces the number of analog to digital converters (ADCs) that are required to drive each mirror from four to just two, but adds analog switches.

This approach shifts most of the complexity of the servo design to the torque inversion problem. However, there is no simple way of measuring the capacitances $C(\alpha,\beta)$, and thus some modeling simplifications have to be made. We can treat the torque functions $f(\alpha,\beta)$ and $g(\alpha,\beta)$ as empirical tables, and use experimental techniques under static conditions to measure them.

We assume that the quadrant capacitance has the following functional form:

$$C(\alpha,\beta) = \sum_{i,j=0}^{n} a_{ij}\,\alpha^i \beta^j + \frac{p}{\left[1-\frac{(\beta+x_0)}{t_x}\right]^{K_X}\left[1-\frac{(\alpha+y_0)}{t_y}\right]^{K_Y}} \quad (3)$$

This form yields torques that behave in a physically intuitive way, i.e., they are monotonic with angles and diverge when the angles approach "touchdown". The parameters a_{ij}, x_0, y_0, p, K_X and K_Y can be found by performing a nonlinear fit of measured static angles for given voltages $V_{1..4}$ and the angles calculated from (1) and (2):

$$\begin{aligned} \beta &= \frac{f(\alpha,\beta)V_4^2 + f(-\alpha,\beta)V_3^2 - f(-\alpha,-\beta)V_2^2 - f(\alpha,-\beta)V_1^2}{K_X} \\ \alpha &= \frac{g(\alpha,\beta)V_4^2 - g(-\alpha,\beta)V_3^2 - g(-\alpha,-\beta)V_2^2 + g(\alpha,-\beta)V_1^2}{K_Y} \end{aligned} \quad (4)$$

The only caveat is that for this procedure to be effective, data of the form $(\alpha,\beta,V_{1\ldots4})$ have to be measured for sufficiently large angles, in particular, larger than the snapdown angles. This regime can only be accessed with the servo controller in place. Therefore, we first carry out a numerical estimate of the capacitance $C(\alpha,\beta)$ and use the derived torques to servo the mirror to some angle past snapdown. This servo operation has degraded dynamical properties, but it provides enough stability to measure the required data up to ~6°. When the final controller is operational with the correct torques, the mirror can be moved to ~8° with the designed dynamics and stability.

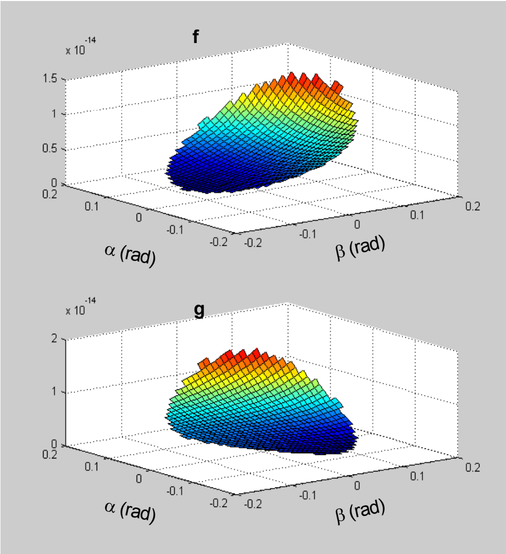

Figure 7: Experimental torque functions *f* and *g*

Figure 7 shows a three-dimensional representation of a typical quadrant torque found using the procedure described before. These torques are finally calculated at a finite grid of 0.25-0.5° and stored into appropriate matrices in the controller code. Torques for angles not on the grid are calculated by linear interpolation.

IV. SERVO CONTROL DESIGN

The main performance parameters required from the servo-controlled mirror are i) the switching time is <10 ms (with the mirror angle within 150 μrad of target angle), ii) the maximum angular deviation due to noise is < 75 μrad per axis, iii) noise rejection and vibration immunity, and iv) a finite available control voltage of less than 85V.

We use state space techniques to design a digital controller with full-state feedback. The choice of sampling frequency is not such a simple task. As a rule of thumb, this value is commonly chosen to be ~10 times higher than the desired system response frequency. At first sight, it would seem that a sampling frequency of the order of a few kHz could be sufficient for this task, providing enough phase margin to account for system non-idealities. The issues of torque inversion and nonlinear behavior under finite sampling time, however, impose stricter restrictions on the stability of the system. Because such issues are difficult to quantify, some experimentation needs to be carried out within the usual controller design guidelines. From our measurements, we obtain satisfactory results for sampling frequencies between 10 and 20 kHz.

A schematic representation of the controller design is shown in Figure 8. A current estimator is used to estimate the angular position and velocity of each mirror axis. In addition, we include an integrator and a feed-forward term to compensate for the extra pole introduced by the integrator [22]. We choose the controller poles at 200 Hz (leading to switching times of the order of a few milliseconds) with estimator and integrator poles 4 to 6 times faster, and a damping ratio of 1, which provides no angular overshoot.

After the torques, T_X and T_Y, are calculated by the servo controller, the torque inversion procedure outlined in the previous section is carried out, leading to the instantaneous values of V_1, V_2, V_3, and V_4. These values are then applied to the corresponding electrodes through the DAC.

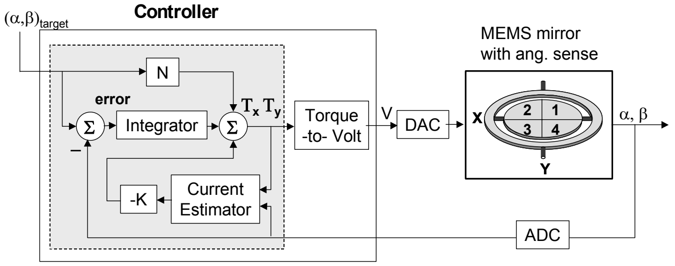

Figure 8: Servo Controller block diagram

V. RESULTS AND DISCUSSIONS

A. *Single Mirror Closed-loop Mirror Performance*

1) *MEMS test setup*

We first evaluate the performance of a single MEMS mirror in an optical tabletop setup to verify and refine the controller design, and to obtain the electro-mechanical characteristics of the individual mirror, such as the angle-voltage relationship and electrostatic torque functions $f(\alpha,\beta)$ and $g(\alpha,\beta)$, needed for building the optical switching system.

We implement an optical method for detecting the mirror angular position. A collimated diode laser beam is incident on the mirror surface at 10° with respect to the fixed substrate normal, and is deflected by the mirror onto a 20-mm-wide position-sensitive detector (PSD). The mirror tilt angles along each axis are, therefore, calculated from the PSD readouts. The PSD is placed about 30 mm away from the MEMS mirror, which permits a maximum of 9° mirror tilt angle to be measured. The PSD output has a very low noise that is equivalent to tens of μrad precision for the detected angle.

A Matlab xPC-target control program is used to implement the close-loop control algorithm and interfaces with a four-channel high-voltage amplifier with a 12-bit DAC for driving the mirror, and interfaces with the PSD output with a 16-bit ADC for mirror angle detection. The MEMS open-loop characteristics are also obtained with the same setup.

2) *Closed-loop Servo Results*

A comparison between open and closed loop switching is shown in Figure 9 for single axis switching.

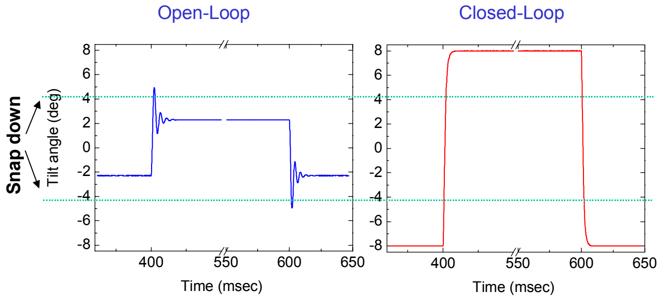

Figure 9: Comparison of switching under open loop and closed loop operation. The closed loop angular trajectory can exceed the snapdown angle and shows no overshoot.

It is evident that the servo controller removes the angular limitation imposed by the instability past snapdown. The touchdown angle for this axis is 10.3 degrees, and thus we were able to servo successfully up to 80% of the angular range. The maximum angle that can be achieved with such controller is limited by the reduction of phase margin caused by the finite sampling time combined with the mirror moving in the unstable regime. Other factors, such as modeling imperfections, neglected resonances, etc., can contribute too. Despite the short switching time, the maximum voltage under servo operation never exceeds 85V throughout the servoed angle range.

Steady-state voltages for each electrode for different tilt angles within a 9-degree cone are also measured. The maximum steady state voltage is about 81V. Note that the values of the required steady-state voltages for this large range of angles can be experimentally obtained only with the aid of the closed-loop servo.

The most stringent measure of success is the steady state angular noise. We record the peak angular noise around the target angle over a period of several minutes, and for a full mesh of angles spanning ±7° for both axes. This noise is recorded using the same angular sense circuitry used for servo control, which provides an additional 25-50 μrad noise coming from this circuitry alone. The peak-to-peak noise map is shown in Figure 10. The optical power stability requirement (<0.5dB) mandates that the angle stability for a single mirror must be better than 150 μrad around the target angle. This corresponds to a maximum of 300-μrad peak-to-peak noise requirement, a number easily met by our controller and plant.

We also tested the robustness of the servo controller against the variations of mirror resonance frequencies and torque tables. We find that for the tested mirrors having ±20% variations in these values, the controller functions essentially the same by using only one set of parameters, which included torsional frequencies, Q, spring stiffnesses, moment of inertia of the mirror and gimbal, $f(\alpha,\beta)$, and $g(\alpha,\beta)$. The robustness of the controller significantly facilitates its implementation by eliminating the necessity of adjusting controller parameters for each specific mirror within a certain range.

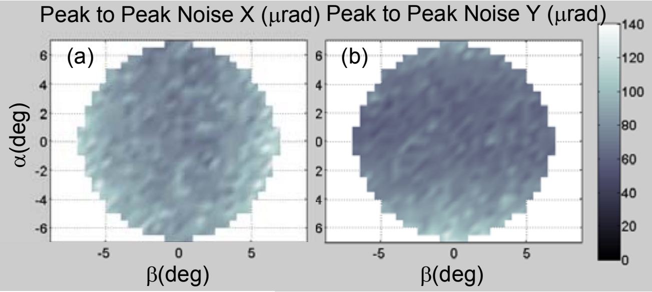

Figure 10: A colormap representation of the peak to peak noise under servo operation and for both axes.

B. Modular Optical Crossconnect with MEMS Mirrors

1) Optical crossconnect Setup

We use these closed-loop controlled mirrors to build a free-space modular optical switch [23]. A schematic diagram of the optical path consisting of optical heads is shown in Figure 11, representing the architecture for a 350 ×350 modular optical cross-connect. Each optical head is composed of a fiber with a fused lens, a fixed folding mirror, a MEMS mirror, a collimating lens, and an optical angle-sensing unit (not shown in the figure) measuring up to 7°. The total optical path between the transmitting and receiving ports is ~2 m and the collimated beam diameter is ~2 mm. Details of this optical architecture are described in reference [23].

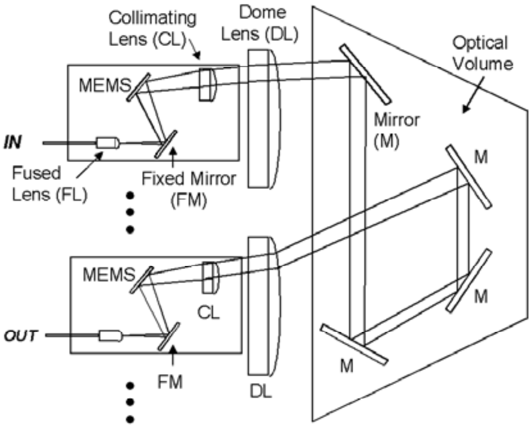

Figure 11: A schematic diagram of the optical path consisting of two optical heads (optical angle-sensing unit is not shown).

An out-of-band beam is employed for sensing the MEMS tilt angles. The optical angle-sensing unit in each optical head is composed of a dichroic beam splitter located between the MEMS mirror and the collimating lens, a set of focusing lenses, a position-sensitive detector (PSD), and supporting electronics. For an input port, the co-propagating data and angle-sensing beams at wavelengths 1310 nm and 980 nm, respectively, exit the input fiber and are reflected by the fixed and MEMS mirrors. These beams are then separated by the dichroic filter, which passes the data beam with negligible loss and reflects fully the out-of-band beam into a PSD through a set of focusing optics. A similar setup is used in a receiving port, except the data and the angle-sensing beams are propagating in opposite directions [23].

2) Hardware Setup for Servo Control

The servo control coding is implemented using a 100MHz 600FLOPS (32-bit floating point) digital signal processor (ADSP-21161N) with interfaces to multiple ADC and DACs (16/12 bit resolution). After code optimization, a single DSP could servo 8 mirrors with a sampling rate of 20KHz (or 16 mirrors at 10KHz). The signal from the PSD in the optical angle-sensing unit for each MEMS mirror is pre-amplified and manipulated in an analog fashion to obtain meaningful angles [24]. A quad-voltage amplifier takes the low voltage output of the DACs and converts them to the appropriate level required to drive the mirrors. As mentioned before, the use of a closed-loop controlled mirror allows the use of a smaller gap between mirror and actuators, thus reducing necessary driving voltage considerably. Therefore, voltage amplifiers with a maximum output of 85V (as opposed to 200-300V usually required by open loop designs [3]) satisfy our requirement.

3) Optical Alignment

An optical connection is established by accurately aligning the input and output port MEMS mirrors. The optical alignment procedure is as follows: For each input port and output port combination, the theoretical pointing angles for each pair of MEMS mirrors are computed based on the ideal geometric locations and optical parameters of the various relevant optical components. Mirror curvature, focal length of lenses, and optical path lengths are all taken into account. These calculated angles serve as starting angles for a four-dimensional peak-search algorithm that determines the best pointing angles based on optimizing the coupling power for a given connection [23]. The four dimensions are from the two tilting angles of both input and output mirrors. The optimized angles are then stored in a look-up table for each connection.

4) *Optical Crossconnect Performance*

Figure 12 (a) shows a fiber-to-fiber switching event commanded to a pair of mirrors. The switching time, as determined from the fiber-coupled optical power, is of the order of 5 ms, and was fairly independent of the angular swing (this is expected in a closed-loop design). When both mirrors are under closed loop control and establishing a connection, the fluctuations in the optical power are of the order of 0.1-0.2 dB, which are very close to the target values. This is shown in Figure 12 (b).

Results as shown in Figure 12(a) is normalized to the optimal steady-state transmitted power of that optical connection. Note that the best total optical loss for a given connection is independent of the performance of the servo system. Instead, it is dependent on the optical components' quality, packaging, and assembly, path length, and mirror angles. The theoretical optical loss for our optical configuration is 2.5 ± 0.5dB for all possible connections, taking into consideration of various loss mechanisms including MEMS mirror etch holes, spring area, and variation in MEMS mirror radius of curvature (20-60cm). Using prototype mirrors with gold coating on only 85% of the mirror surfaces, the measured losses were 6.0 dB ± 1.0 dB, close to the predicted value of ~5.5 dB [23].

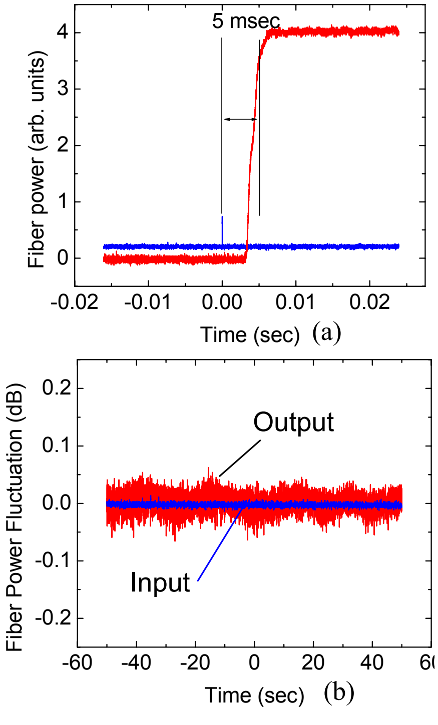

Figure 12: (a) A fiber-to-fiber switching event as observed through the fiber-coupled optical power when two ports establish a connection. (b) Optical power stability under a stable connection. The angles used for these measurements were close to 5 degrees, which is beyond snapdown.

While the PSD optical feedback systems could achieve excellent performance in pointing each mirror to a target angle, a given pair of target angles does not always yield optimal coupling power due to thermal mechanical drift of the whole optical train. Electronics drift (in PSD sensor or amplifier) may also invalidate the target angle values. To compensate for slow thermally-induced drift, power measurements taken at 1-kHz rate are used to trigger the peak-search algorithm whenever the optical loss is greater than a selected threshold (such as 0.4dB) in order to determine new optimal pointing angles. With this "dual" feedback system, long term optical power stability of better than 0.5 dB at 21°C ± 4°C is possible by properly setting the peak-search threshold and step-size.

The optical power sensitivity to temperature change is also strongly dependent on the MEMS mirror curvature, and thus, to the deposition temperature of the reflective coating and the nominal operation temperature of the MEMS mirror. Retargeting of the MEMS mirrors, however, cannot compensate for coupling loss contributed by mirror curvature change due to temperature. Fortunately, optimization of the mirror-coating process as well as temperature control of the switch fabric can minimize this loss mechanism.

VI. CONCLUSION

We demonstrate full closed-loop control of electrostatically actuated MEMS mirrors and their performance in a free space optical crossconnect. The mirror fabrication process, actuation method, and spring designs are presented. A state space controller is developed to implement the non-linear control of the mirrors. The mirror angular operation range is extended to 80% of the mirror touchdown angle, well beyond its snapdown angle. Long-term angular noise of less than 150 µrad is also achieved. We use these closed loop controlled mirrors in a free space optical crossconnect, and achieve switching times less than 10ms and optical power stability of better than 0.2dB.

REFERENCES

[1] P.B. Chu, S.S. Lee, S. Park, "MEMS: The Path to Large Optical Crossconnects," *IEEE Communication Magazine*, Vol. 40, No. 3, pp. 80-87, March 2002.

[2] A. S. Dewa, J. W. Orcutt, M. Hundson, D. Krozier, A. Richards, and H. Laor, "Development of a silicon two-axis micromirror for an optical cross-connect", *Tech. Dig. IEEE Solid-State Sensor Actuator Workshop*, Hilton Head Island, pp. 93-96, 2000.

[3] R. Ryf, et al., "1296-port MEMS transparent optical crossconnect with 2.07 Petabit switch capacity," in *Tech. Dig. Optical Fiber Conference 2001*, Anaheim, CA, 2001.

[4] D. J. Bishop, C. R. Giles, and G. P. Austin," The Lucent LambdaRouter: MEMS technology of the future here today," *IEEE Communication Magazine*, Vol. 40, No. 3, pp. 75-79, March 2002.

[5] J.H. Smith, S. S. Nasiri, J. Bryzek, M. Novack, J. B. Starr, H. Kwon, A. F. Flannery, D. L. Marx, Z. Chen, and E. Sigari, "1200 Mirror Array Integrated with CMOS for Photonic Switching: Application of Mechanical Leveraging and Torsional Electrostatic Actuation To Reduce Drive Voltage Requirements and Increase Angular Tilt", *Tech. Dig. IEEE Solid-State Sensor Actuator Workshop*, Hilton Head Island, pp. 378-379, 2002.

[6] O. Degani, et al., "Pull-in study of an electrostatic torsion actuator", *IEEE JMEMS*, **7**(4), pp. 373-378, 1998.

[7] Y. Nemirovsky and O. Bochobza-Degani, “A Methodology and Model for the Pull-In Parameters of Electrostatic Actuators”, *IEEE JMEMS*, 10(4), pp. 601-615, 1998.

[8] P.B. Chu, K.S.J. Pister, “Analysis of Closed-Loop Control of Parallel-Plate Electrostatic Microgrippers,” Proc IEEE Int. Conf. On Robotics & Automation, San Diego, CA, pp. 820-825,1994.

[9] M.S.-C. Lu and G. K. Fedder, “Closed-loop control of parallel-plate microactuator beyond the pull-in limit,” *Tech. Dig. IEEE Solid-State Sensor Actuator Workshop*, Hilton Head Island, pp. 255-258, 2002.

[10] E.S. Hung and S.D. Senturia, “Extending the Travel Range of Analog-Tuned Electrostatic Actuators”, *IEEE JMEMS*, 8(4), pp. 497-505, 1999.

[11] T.D. Kudrle, *et. al*., “Pull-in Suppression and Torque Magnification in Parallel Plate Electrostatic Actuators with Side Electrodes”, *Proc. 12th Int. Conf. On Solid State Sensors, Actuators and Microsystems*, Boston, 2003, pp. 360-363.

[12] C. Pu, S. Park, P. Chu, S.-S. Lee, M. Tsai, D. Peale, N. Bonadeo, and I. Brener, “Electrostatic actuation of 3-D MEMS mirrors by sidewall electrodes,” Proc. Int. Conf. on Optical MEMS and Their Applications, Waikoloa, Hawaii, 2003.

[13] I. Brener, *et. al*, “Nonlinear Servo Control of MEMS Mirrors and Their Performance in a Large Port-Count Optical Switch”, Proc. OFC, 2003, vol.1, 385-386.

[14] T. Juneau, K. Unterkofler, T. Seliverstov, S. Zhang, M. Judy, “Dual-axis optical mirror positioning using a nonlinear closed-loop controller”, *Proc. 12th Int. Conf. On Solid State Sensors, Actuators and Microsystems*, Boston, 2003, pp. 560-563.

[15] N.Yazdi, H. Sane, T.D. Kudrle, and C.H. Mastrangelo, “Robust Sliding-mode Control of Electrostatic Torsional Micromirrors Beyond the Pull-in Limit”, *Proc. 12th Int. Conf. On Solid State Sensors, Actuators and Microsystems*, Boston, 2003, pp. 1450-1453.

[16] S.Blackstone and T.J. Brosnihan, *Proc. IEEE/LEOS Int. Conf. Optical MEMS ‘01*, Okinawa, Japan, 2001, pp. 35-36.

[17] T.J. Brosnihan, *et. al*, “Optical IMEMS – A fabrication process for MEMS optical switches with Integrated on-chip electronics”, Proc. 12th Int. Conf. On Solid State Sensors, Actuators and Microsystems, Boston, 2003, pp. 1638-1642.

[18] K.E. Petersen, “Silicon as a Mechanical Material”, Proc. IEEE, vol. 70, 1982, pp. 420-457.

[19] P.B. Chu, et al, “Controlled Pulse-Etching with Xenon Difluoride,” *Proc. 9th Int. Conf. On Solid State Sensors, Actuators and Microsystems*, Chicago, 1997, pp. 665-668.

[20] X. Wang, M. Judy, J. White, “Validating fast simulation of air damping in micromachined devices”, in *Tech. Digest of 15th IEEE Int. Conf. on MEMS*, 1999, pp. 210-213.

[21] T. Roessig, “Mirrors with integrated position-sense electronics for optical-switching applications,” *Analog Dialogue* by Analog Devices Inc. (www.analog.com), vol. 36, no. 4, July-August, 2002.

[22] G.F. Franklin *et al.*, *Digital Control of Dynamic Systems*, Addison Wesley, Menlo Park, California, 1998, pp.323-325.

[23] J. I. Dadap, P. B. Chu, I. Brener, C. Pu, C. D. Lee, K. Bergman, N. Bonadeo, T. Chau, M. Chou, R. Doran, R. Gibson, R. Harel, J. J. Johnson, S. S. Lee, S. Park, D. R. Peale, R. Rodriguez, D. Tong, M. Tsai, C. Wu, W. Zhong, E. L. Goldstein, L. Y. Lin, and J. A. Walker, “Modular MEMS-based optical cross-connect with large port-count,” *IEEE Photonics Technology Letters*, vol. 15, no. 12, 2003, pp. 1773-1775.

[24] Y. Reznichenko, M. Judy, S. Zhang, “Measuring the optical and electromechanical properties of MEMS mirrors,” Proc. 12th Int. Conf. On Solid State Sensors, Actuators and Microsystems, Boston, 2003, pp. 1466-1469.